17

Emerging Maskless Nanolithography Based on Novel Diffraction Gratings

Guanxiao Cheng[1,2,3], Yong Yang[4], Chao Hu[2,3,5], Ping Xu[1], Helun Song[6], Tingwen Xing[4] and Max Q.-H. Meng[2,3]
[1]*College of Electronic Science and Technology, Shenzhen University, Shenzhen,*
[2]*Shenzhen Institutes of Advanced Technology, Chinese Academy of Sciences, Shenzhen,*
[3]*The Chinese University of Hong Kong, Hong Kong,*
[4]*Institute of Optics and Electronics, Chinese Academy of Sciences, Chengdu,*
[5]*Ningbo Institute of Technology, Zhejiang University, Ningbo,*
[6]*Suzhou Institute of Nano-tech and Nano-bionics, Chinese Academy of Sciences, Suzhou, China*

1. Introduction

The development of lithographic technology that has been used in semiconductor electronics has led to systems that put a premium on spatial resolution, throughput and reliability, regardless of cost and flexibility. According to Abbe's theory, the spatial resolution can be improved by using either shorter wavelength or higher numerical aperture (*NA*). Although the semiconductor industry has made significant progress in increasing the lithography resolution in the past decades, further improvement of the resolution by accessing shorter wavelengths is facing critical challenges due to the availability of optical materials with suitable refractive index. The expansion of nanoscale science and engineering will require flexible, high spatial resolution, and low-cost nanolithographic techniques and systems other than those employed in the semiconductor industry, for reasons of both cost and limited flexibility. The research on Emerging Maskless Nanolithography Based on Novel Diffraction Gratings presented in this chapter is a step in the direction of providing affordable, highly flexible nanolithography.

In this chapter, we present two cases for maskless nanolithography employed novel diffraction optics elements as objective lens to focus illumination light. The diffractive objective lens (DOL) operates by the principle of diffraction other than conventional objective lens functioning by refraction. DOL can be designed to operate at any wavelength while refractive elements are constrained at short wavelengths by material transmission properties. DOL are thinner, and can be fabricated by planar techniques that are reliable and low cost.

DOL, in a form of photon sieves originally used in x-ray microscopy and achieved 6nm resolution, is possible to extend the use of diffractive elements down to the limits of nanolithography. Recently, we present the scheme of photon sieve array X-ray maskless nanolithography (PSAL) to fabricate novel nanometer devices (Cheng et al., 2006, 2007a, 2007b, 2008). The lithographic principle is shown in figure 1. Firstly, each of the photon sieve

array focuses incident X-ray into a diffraction-limited on-axis spot on the surface of a photoresist-coated substrate, the X-ray intensity of each spot is modulated by means of a spatial light modulator. Then, patterns of arbitrary geometry are written in a dot matrix fashion while the photoresist-coated substrate on a precision stepping stage is exposed to the properly modulated X-ray.

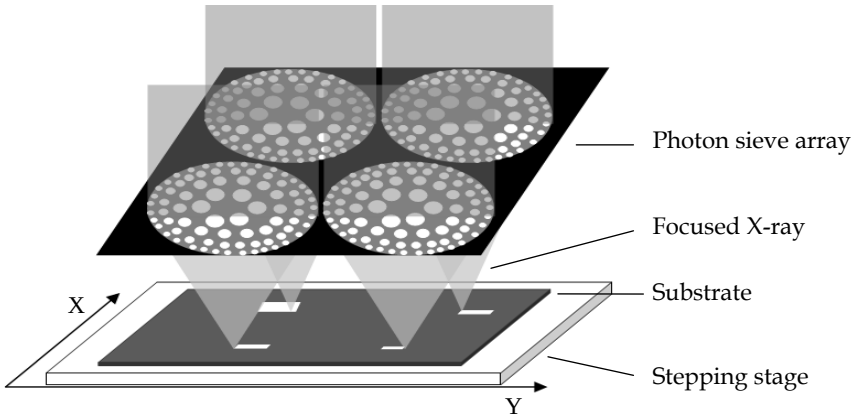

Fig. 1. Schematic of PSAL. An array of photon sieves focuses incident X-ray into a matrix of spots on the substrate coated photoresist. Patterns of arbitrary geometry are recorded while the stepping stage is driven.

In combination with the synchrotron light sources, PSAL can offer a new lithographic tool for high-resolution X-ray nanolithography in physical and nanoscale sciences. The PSAL lithographic system will be further discussed in detail on the synchrotron radiation light, resolution limits, depth of focus, etc. The design, fabrication, and experimental characteristic of X-ray photon sieve will also be illustrated by numerical analyse and experimental results. According to Fresnel-Kirchhoff diffraction theory, the diffractive field of photon sieve is described by means of the discrete fast Fourier transform algorithm. The approaches to enhancing imaging resolution of photon sieve are presented in detail. The related contents include the calculation of point spread function, the suppression of side lobes, the imaging bandwidth, the physical limit of resolution, and the diffraction efficiency. Imaging properties of photon sieve are analyzed on the basis of precise test and shown that photon sieve is a kind of diffractive optical element modulating either amplitude or phase and thus suffers from chromatic aberration or low diffraction efficiency. Hybrid lens consisting of both refractive optical surfaces and photon sieve are suggested to correct the chromatic aberration. Phase-photon sieve technology and surface plasmon polaritons technology are promising approaches to improve the diffraction efficiency and spatial resolution.

DOL, in another form of superlens consisted of nano-filmed noble metals on which the evanescent field is strongly enhanced using the resonant excitation of surface plasmons that can be excited at given conditions, is also possible to extend the use of diffractive elements down to the limits of nanolithography (Yang et al., 2007a, 2007b, 2009). The high-resolution plasmonic nanolithography has been investigated by using optical proximity exposure in the evanescent near field in nano-filmed noble metals. Sub-diffraction-limited feature size

can be resolved by using I-line illumination exposure. Compared with the model of original superlens, we separated the superlens 100nm away from the substrate, under the illumination of I-line light, the initial simulation shows that the sub-diffraction-limited feature as small as 60nm line width with 120nm pitch can be clearly resolved without hard contact between the substrate and the superlens. This is shown in figure 2. By proper design of the materials and the parameters of nano-filmed layers, better resolution can be realized.

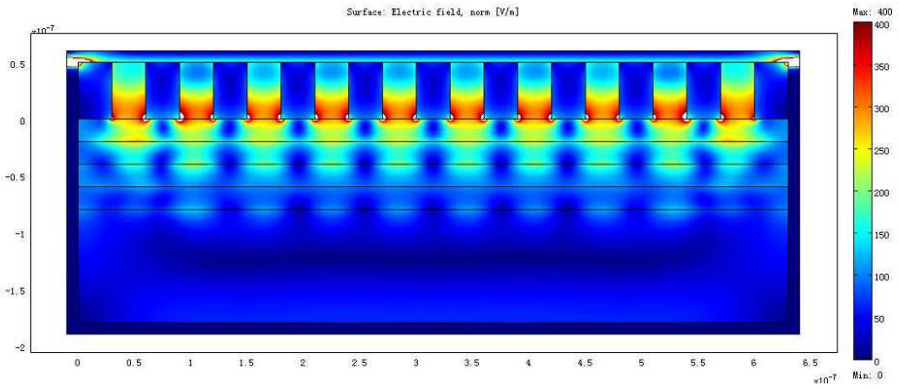

Fig. 2. Electric field distribution of dual-layered heterostructure for CD=30nm.

2. Photon sieve array X-ray maskless nanolithography

Lithography has been the key technology in the semiconductor industry. Beyond the semiconductor industry, lithography has also been widely employed in such technological fields as microoptics, nanophotonics, MOEMS, nanotechnology, etc. In order to achieve the minimum feature size, the development of lithography has resulted in setups with high throughput and reliability regardless of cost and flexibility.

For nanoscale science and engineering, however, the lower cost and higher flexibility of lithography must be considered. Fortunately, maskless lithography can meet the requirements of nanotechnology. There are various forms of maskless lithography that include scanning electron-beam lithography, focused ion-beam lithography, multiaxis electron-beam lithography, interference lithography, maskless optical-projection lithography, scanning probe lithography, zone plate array lithography (ZPAL) (Menon et al., 2005), etc. It is a very complex process of selecting an optimum lithography tool that requires knowledge and experience in several disciplines including physics, chemistry, electronics, device design, manufacturing, processing, cost and marketing. Although the selection strategy consists of many aspects, the technical aspect is the dominant item because the tool has to be technically performable. Menon et al. showed the feasibility of ZPAL operating at a wavelength of 400nm and its potential for the fabrication of novel devices.

Photon sieve is a novel diffractive optical element which consists of a great number of pinholes distributed appropriately over the Fresnel zones for the focusing and imaging of soft X-rays (Kipp et al., 2001). Photon sieve has advantages of the diameter of pinholes beyond the limitation of the corresponding Fresnel zone width and the minimum background in the focal

plane, which is shown in figure 3. The focal spot produced by a Fresnel zone plate is surrounded by rings of intensity (secondary maxima) that blur the images. For a zone plate, each ring contributes equally to the amplitude at the focus. This contribution drops abruptly to zero beyond the outermost ring which leads to strong intensity oscillations in the diffraction pattern (top row). With a photon sieve, the number of pinholes per ring can be readily adjusted to yield a smooth transition which minimizes the secondary maxima (bottom row). This provides sharper images. Note that diffraction intensities are plotted on a log scale (right column). Furthermore, photon sieve can be fabricated on a single surface without any supporting struts required unlike the Fresnel zone plate.

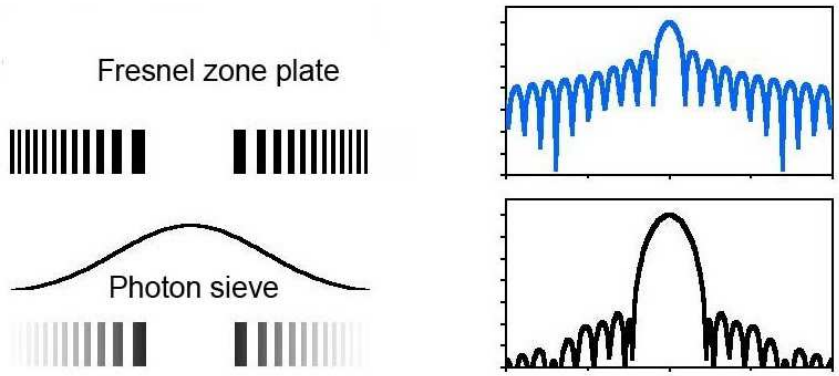

Fig. 3. Schematic of photon sieve suppressing side lobes.

In this section, we present the scheme of maskless nanolithography using a large array of photon sieves, each of which focuses incident X-ray into a diffraction-limited on-axis spot on the surface of a photoresist-coated substrate (PSAL). The X-ray intensity of each spot is modulated by means of a spatial light modulator. Patterns of arbitrary geometry are written in a dot matrix fashion while the photoresist-coated substrate on a precision stepping stage is exposed to the properly modulated X-ray. In combination with the synchrotron light sources, PSAL can offer a new tool for high-resolution X-ray nanolithography in physical and nano sciences. Lastly, the design and fabrication of photon sieve are illustrated with a low-*NA* amplitude-photon sieve fabricated on a chrome-coated quartz plate using laser-beam lithographic process.

2.1 Scheme of photon sieve array X-ray maskless nanolithography

In PSAL system operating at wavelength of 0.5~2nm synchrotron light sources radiated, each of a large array of photon sieves focuses incident X-ray into a diffraction-limited on-axis nanoscale spot on the substrate coated photoresist. Patterns of arbitrary geometry are exposed in a dot matrix fashion while the substrate on a stepping stage is precisely driven in two dimensions according to the computer program. A Schematic of PSAL is shown in Figure 1. PSAL provides a promising approach for the fabrication of nanometric device and integrated circuit (IC). There are emphases on light source, resolution, depth of focus and process latitude in both nanodevice and the IC areas. In the section, we will go into detail the four characteristics.

2.2 Source of X-ray

PSAL utilizes very short wavelength synchrotron radiation source emitted. Synchrotron radiation arises from the changing direction of a high energy relativistic beam of electrons caused to run a circular modified elliptical path. The key characteristics of synchrotron radiation light are high brightness, very small divergence, extremely narrow bandwidth, and so on. In the case of synchrotron radiation, the operating wavelength ranged from 0.5nm to 2nm is very suitable for nanolithographic research.

2.3 Resolution

Resolution limits are caused by the diffraction effects and photoelectron spreading. On one hand, the minimum diffraction-limited resolution of a PSAL system is determined by

$$R_{\min} = k_1 \lambda / NA \tag{1}$$

where λ is the exposure wavelength of the incident light, k_1 is a factor between 0.5 and 1. The shortest exposure wavelength contemplated is 0.5nm. NA of approximately 0.8 is expected. As a result, the minimum feature size R_{min} for such a system may approach 0.3nm. Therefore, PSAL is very promising for the fabrication of nanodevices.

On the other hand, the incident x-ray photon usually transforms all its energy into a single high energy photoelectron in the incident solid. Both a secondary electron shower and the chemical alterations in photoresist necessary for exposure are caused by this primary photoelectron. Therefore, resolution limits arise also from the range of this photoelectron.

2.4 Depth of focus

The depth of focus (DOF) of a PSAL system is given by

$$DOF = \pm k_2 \lambda / NA^2 \tag{2}$$

where k_2 is determined by the lithography process in use, ranging from 0.5 to 1. DOF defines the maximum tolerable displacement of the image plane from its ideal position. The approach to optically polishing imaging surfaces tends to make lithography easier by eliminating depth-of-focus problems. For example, a photon sieve of NA = 0.8 and k_2 = 0.6, operating at 2 nm, the DOF is $\pm 1.9nm$.

2.5 Process latitude

If tiny variations in exposure and development conditions cause large varieties in the exposed pattern, the process is worthless. Process latitude is defined that the variety of some critical process parameters (such as line width, edge acuity, etc.) concerning the processing conditions (such as exposure time, development time, etc.). Ideally, a process whose critical parameters change as little as possible for a given change in process condition is desired.

2.6 Design of photon sieve

Photon sieve can produce effects on their own depending on what the optical engineer is trying to achieve for a particular design goal. In situations where size or weight are critical, photon sieves bring substantial advantages. The flexibility in constructing wavefronts gives an optical designer the ability to use photon sieves fabricated microscopic structures on flat surfaces as converging lenses all by themselves. Acted as a diffractive optical element,

photon sieves can also be used to correct image aberrations and color aberrations in a lens in a manner similar to the use of aspheric surfaces and additional refractive components. For example, the hybrid lens, consisting of a photon sieves with a conventional refractive lens, can provide the required color correction.

One useful method of the approaches to designing photon sieve is the paraxially individual far-field model and the nonparaxial model (Cao & Jahns, 2002, 2003). The former derived from the paraxial Fresnel diffraction is valid for the low-NA photon sieve. The latter based on the nonparaxial expression for the far field of individual pinholes and the linear superposition principle is valid for high-*NA* photon sieve, such as the photon sieves operating in X-ray region.

The key methods designing photon sieve are to optimize positions and radii of pinholes. Kipp et al. pointed out that photon sieve consists of a large number of pinholes distributed appropriately over the zones of a Fresnel zone plate pattern. The size of the focused spot is approximately equal to the width of the smallest zone in the underlying zone plate pattern. The diffracted field of a single pinhole can be expressed as

$$U \propto KJ_1(0.5\pi K) \tag{3}$$

where K is the ratio of pinhole diameter to the corresponding zone width and J_1 is the first order Bessel function of the first kind. The maximum modulus of U appears when K is approximately equal to 1.5, 3.5, 5.5, etc, as shown in figure 4. The parameter K may be utilized to relax the fabrication requirements for the photon sieve considerably as compared with a zone plate of the same *NA*.

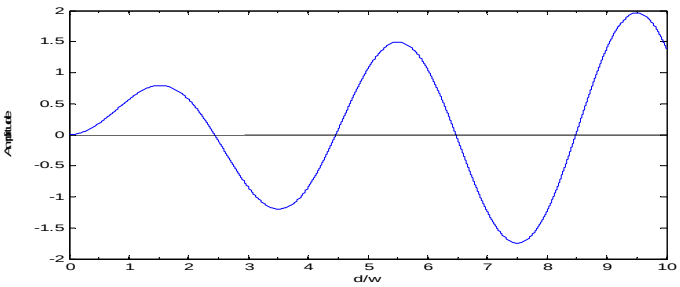

Fig. 4. The diffracted field of a single pinhole.

The point-spread function (PSF) of a traditional Fresnel zone plates generally has side-lobes of noticeable strength. The side-lobes blur the image obtained by the zone plates. The photon sieve may create a PSF that has lower side-lobes at the expense of a slightly wider main lobe than the zone plates. Moreover, an additional benefit of the photon sieve is that it breaks the periodicity that is inherent in the zone plates, thus strongly attenuating the higher diffracted orders. For an amplitude-photon sieve, apodization may be achieved by varying the transmissivity of its pupil gradually, i.e., the number of its pinholes, as a function of radial distance so as to follow approximately the function form of a Gaussian distribution

$$G(r) = \exp(-0.5r^2/\sigma^2) \tag{4}$$

where r is the radius at the center of the underlying zone pattern and is the parameter that controls the strength of apodization. The apodization parameter may be adjusted to achieve the optimum desired intensity distribution at the focal plane (Cheng et al., 2010, 2011).

We calculated the PSF intensity distribution of photon sieves with different apodization parameters at focal plane compared with a zone plates. Figure 5(a) shows a plot of the pupil intensity transmission of a zone plate with rectangular transmission window and two photon sieves with Gaussian transmission windows $(\sigma = 1, 0.5)$, respectively. In fact, the rectangular transmission pupil can also be derived from the Gaussian transmission pupil when $\sigma = \infty$. Figure 5(b) shows cross sections of the intensity PSF for the three cases. The logarithm of intensity is plotted vertically in order to emphasize the side-lobes, and the intensity normalization is proportional to the total integrated intensity passed by the pupil in each case. It may be seen that the Gaussian apodization significantly suppresses the side-lobes at the expense of slightly broadening the main lobe. The relative attenuation of side-lobes of the zone plate and photon sieves is -13.2dB, -16.7dB, -32.8dB, respectively. The full width at half maximum (FWHM) of these main lobes is 0.05, 0.05, 0.07, respectively. Therefore, a less value of σ produces a narrower window and a less strength of side-lobes at the expense of a somewhat wider main lobe.

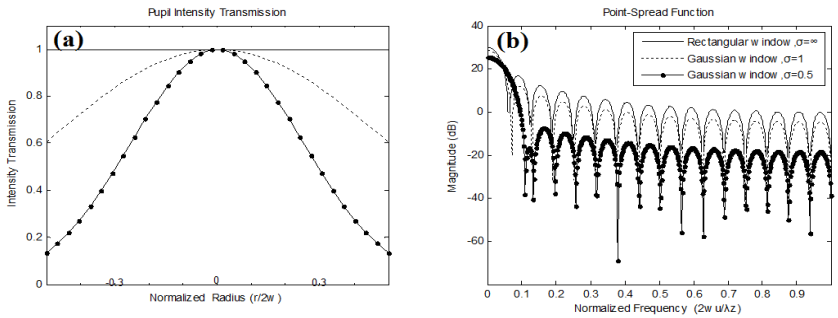

Fig. 5. Comparison of calculated intensity distributions of photon sieves and zone plate with different apodization windows. (a) Transmission windows in pupil plane for a zone plate (solid line) with a rectangular apodization window and two different photon sieves with Gaussian apodization window: σ=1 (dotted line), σ=0.5 (solid-dot line), respectively. (b) Transverse intensity point-spread function distribution in focal plane for the corresponding zone plate and photon sieves.

We designed an amplitude-photon sieve. The diffraction element had a diameter of 30mm and a focus length of 175 mm for an operating wavelength 632.8 nm. The pinholes were distributed over zones of order ranged from 2 to 1000. The minimum diameter of pinhole was 5.6 μm . We give the simulation results of pinhole positions distributed over the zones of order from 2 to 100 and the point spread function of the former 10 zones, which are shown in Figure 6.

A Gaussian apodized X-rays amplitude-photon sieve at a wavelength of 0.5nm (20mm focal length, 2mm pupil diameter, 0.05 *NA*) is simulated based on the scalar diffraction theory. The minimum feature size and total number of pinholes is 7.5nm, 14215227, respectively. The spatial resolution of 6.1nm can be obtained. Figure 7 shows the distribution of central

part of the photon sieve, which the ratio of pinhole diameter to underlying zone width is chosen as 1.5.

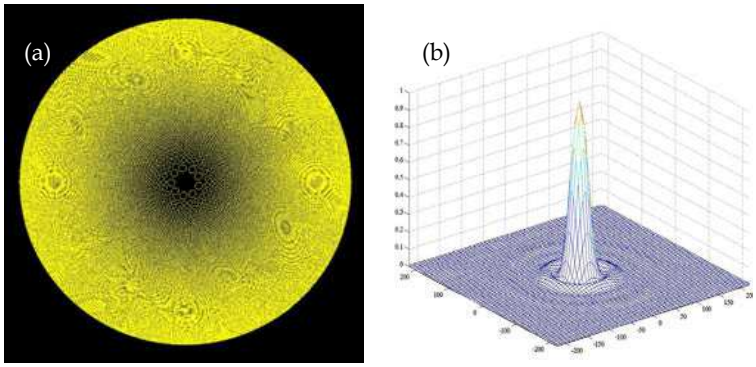

Fig. 6. Simulated pinholes distribution and PSF of a photon sieve.

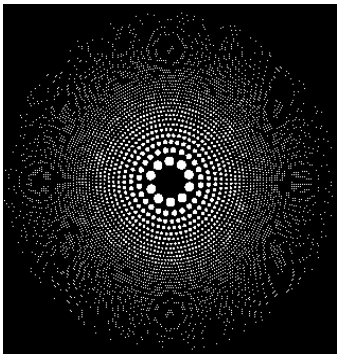

Fig. 7. Pinholes distribution of an apodized X-rays photon sieve.

The diffraction efficiency scales as the square of the transmission area. A photon sieve transmits only 15~30% of the incident light because of the Gaussian apodization whereas an amplitude-zone plate has a transmission of 50%. Therefore, the first-order diffraction efficiency of a photon sieve is lower than that of a zone plate of equal *NA* by a factor of 10. However, the photon sieve is an attractive alternative to conventional zone plates for the X-rays focusing and imaging elements in the situation using the brilliant X-rays from synchrotron light sources as illumination, the diffraction efficiency is not a very important consideration but the side-lobes suppression and the fabrication ease are relatively more important.

The process of designing an amplitude-photon sieve is shown as follows. Firstly, the operating wavelength, diameter and focal length of photon sieve are given according to the purpose of imaging or focusing. Secondly, the number of corresponding Fresnel zones is calculated. Lastly, the optimum radius and coordinate of each pinhole in each corresponding zone are determined, and then the data of all pinholes are stored in the same file in order to create the photon sieve.

2.7 Fabrication and experiment

In order to verify the feasibility of the above methods, we fabricated a Gaussian apodized amplitude-photon sieve (633nm design wavelength, 175mm focal length, 30mm pupil diameter, 0.08 *NA*) on chrome-coated quartz plate using laser-beam lithographic techniques. The resolution image was recorded at 627nm peak-wavelength and 20nm spectral half-width produced by a light-emitting diode. Figure 8 demonstrates the pinholes distribution of the central part of the Gaussian apodized amplitude-photon sieve and the ratio of pinhole diameter to underlying zone width is chosen as 1.5.

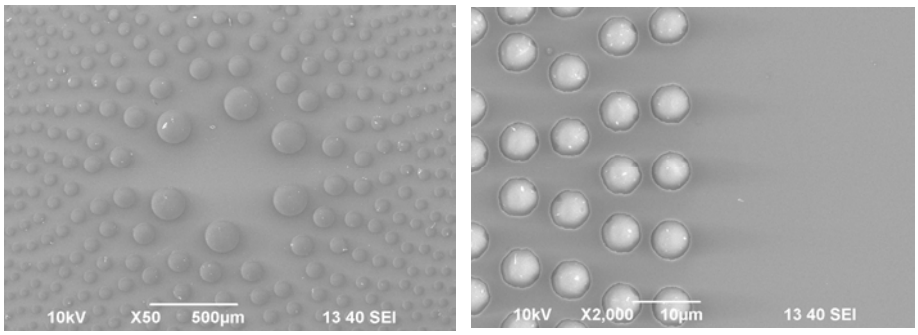

(a) (b)

Fig. 8. Scanning electron microscope images of an amplitude-photon sieve. (a)Central portion, (b)the outermost portion.

For the purpose of testing the imaging property, a beam of even illumination was produced by a light-emitting diode (LED, with peak-wavelength 627nm and spectral half-width 20nm) and a ground-glass diffuser. The beam transmitted through a WT1005-62 resolution test target was then incident upon the photon sieve. The resolution images were recorded by an intensified charge coupled device (ICCD). Figure 9 shows that good agreement between experimental and theoretical results concerning reduction of side-lobes but the resolution of 5.9um obtained is somewhat lower than the expected resolution limit of 4.8um because of the wavelength difference and chromatic aberration.

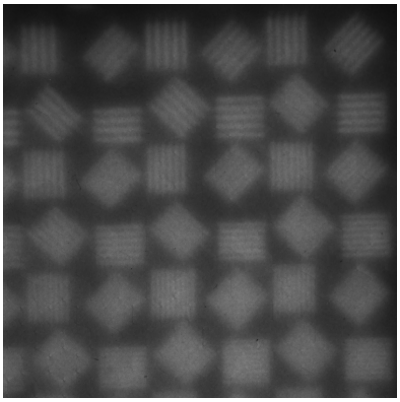

Fig. 9. Resolution test target imaged with an apodized photon sieve at 627 nm.

In brief, the experiment mentioned above demonstrates the feasibility of using photon sieves as the focusing optical element. We believe in that PSAL will be used as one of the promising tools in the nanometric device and special IC areas for the purpose of high resolution regardless of low yield.

3. Nanolithography in the evanescent near field by using nano-filmed noble metal layers

The sharpness of object can't be resolved by conventional lens due to the limitation by the wavelength of illumination light. J. B. Pendry had predicted that a slab of negative refractive index material has the power to focus all Fourier components of a 2D image. The super resolution of the negative index materials using silver layer, which was called 'superlens', can reconstruct the image of a pattern with line width of 40nm (Fang, et al., 2005). They made mask, silver slab and photoresist integrity in Fang's experiment, which likes the traditional contact exposure of lithography. It is not practical in real application by Fang's method of nanolithography because each wafer needs its respective mask. The experiments of super resolution using silver slab was reported, and the line width with one fifth of illumination wavelength can be successfully resolved by the silver slab (Blaikie et al., 2006).

Though Blaikie's experiment made mask and silver integrity, they separated photoresist from silver slab. This kind of configuration still had limitation in practical application. In order to investigate the influence of distance between mask and noble metal slab on imaging, we designed a separated 'superlens' with silver slab 100nm away from mask. We analyzed the distribution of optical field by Finite Difference Time Domain (FDTD). The results show that the images of object can be reconstructed by the structure.

3.1 Nanolithography method

The exposure method of near-field nanolithography that was proposed by this paper is illustrated in Figure 10. A UV transparent substrate with refractive index of n = 1.6 (@365nm) is used for supporting the mask. The object layer with line width of 60nm and pitch of 120nm, which is made of Cr with refractive index of n=2.924 (@365nm), acts as the function of mask in exposure. The air gap comes from the vacuum contact between mask and silver layer, which can be viewed as a kind of practical nanolithography technique.

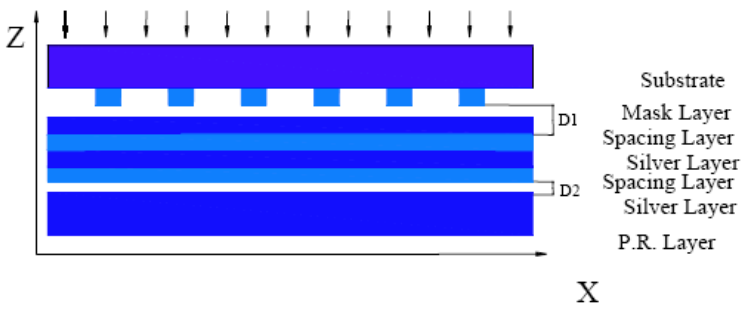

Fig. 10. Sketch of Nanolithography Model.

Materials	Parameters	Thickness
Substrate	Refractive index n=1.6@365nm	100nm
Mask	Refractive index n=2.9@365nm	40nm
Spacing	Refractive index n=1.52@365nm	40nm
Silver	Permittivity $\varepsilon_{Ag} = -2.4 + i0.2488@365nm$	40nm
Photoresist	Refractive index n=1.7@365nm	100nm

Table 1. Physical parameters of the materials in Fig. 10.

In figure 10, the spacing layer with refractive index of n=1.517 (@365nm) acts as the following two functions: 1) to match the surface plasmon polaritons resonating conditions; 2) to protect the surface of silver slab. As for the image recording, we chose the negative photoresist of i-line.

In order to explore the potential valid imaging distance between mask and photoresist, a repeat of spacing layer and silver slab layer was followed after the first silver slab. The sample was exposed in i-line light that shone from the substrate side. For the convenience of description, we defined D1 as the distance between mask and silver slab, and D2 as the distance between silver slab and photoresist.

3.2 When silver slab separated 40nm from mask (i.e. D1=40nm)

In order to save calculating time and PC resources, we computed the distribution of optical near-field intensity by the 2-D FDTD method. We chose cell size of X*Z=2×1(nm), which is much smaller than both the exposure light wavelength and the mask's feature size. The time step, according to Courant condition, should be:

$$TimeStep = 2\sqrt{2}N^{1/3} \tag{5}$$

N is the total cells of computing area. We chose 3500, by which the amplitude of electric field already became steady. The distance of 40nm comes from the spacing layer. At this situation, it is a kind of ideal condition, because mask and spacing layer had a hard contact. The surface plasmons polaritons of two interfaces between silver slab and its surroundings can magnify the evanescent waves that carried the detailed information of object. When D1=40nm, we calculated the following 4 conditions: D2=0nm, 20nm, 40nm, 60nm. Figure 11 show the distribution of electromagnetic (abbreviated to EM afterwards in the paper) field respectively.

It was found that the image of mask can be clear resolved by the method. Figure 11(a) shows better result, however, figure 11(b)-(d) showed worse results due to the exponential decay of the evanescent waves came from the exit side of the interface between silver slab and photoresist. The strong contrast of EM field may come from the edge effect of the evanescent waves. We chose the 10nm cross-section of photoresist layer to compare the imaging result of silver slab. When D1=40nm and D2 varied from 0nm to 60nm, the distribution of optical field in the section was shown in Figure 11. When D2 changed from 0nm to 60nm, the amplitude reduced to about a half under the same condition, but the high contrast of lines still can be clearly observed in figure 12. The amplitudes of lines were relatively uniform when D_2=20nm and 60nm compared with D_2=0nm. If the parameters of photoresist were

under better control, the lines of images will be more uniform. However, compare with the condition of D2=0nm, the depth of lines in photoresist will be shallower at the same exposure condition.

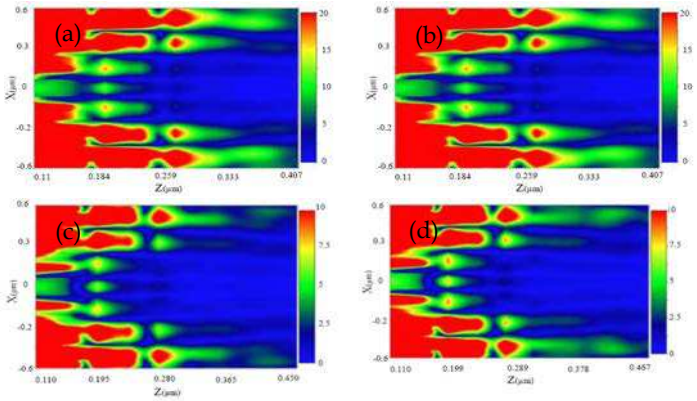

Fig. 11. The distribution of EM field in the model. Photoresist layer lies (a) between Z=0.31μm and Z=0.41μm, (b) between Z=0.33μm and Z=0.43μm, (c) between Z=0.35μm and Z=0.45μm, (d) between Z=0.7μm and Z=0.47μm.

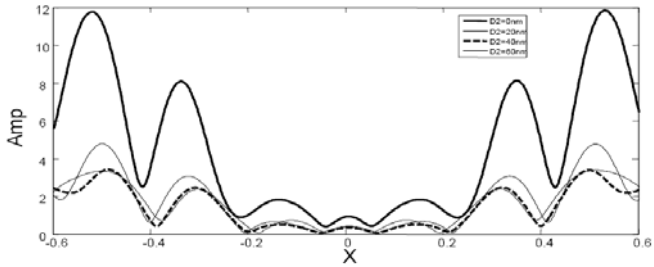

Fig. 12. The distribution of optical field in the 10 nm cross-section of photoresist when D1=40nm.

3.3 When silver slab separated 60nm and 80nm from mask (i.e. D1=60nm, 80nm)

When D1=60nm, 80nm, we calculated 4 conditions respectively for each D1. We still chose the 10nm cross-section of photoresist layer to investigate the optical field. In order to show the clear comparison results, we give the final comparison of the amplitude instead of EM distribution figures for each condition of different D2. Figure 13 and figure 14 showed the result respectively when silver slab separated 60nm and 80nm from mask.

It was found that there came out extra fringes in figure13 and figure 14. This kind of phenomena may be caused by the strong interference effects among evanescent waves. The image of mask still can be resolved in photoresist layer by proper choice of materials and exposure conditions. These results showed a bad conformity between mask and recorded image in photoresist layer. On the other hand, it gave us a hint to realize better resolution of optical lithography by reasonably using the interference effect.

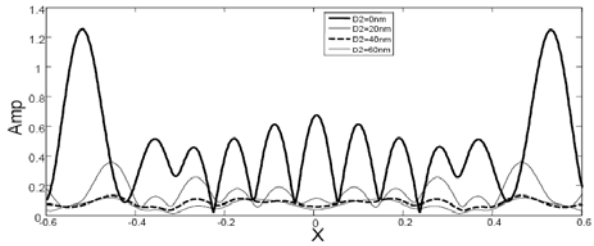

Fig. 13. The final comparison when D_1=60nm while D_2=0, 20, 40 and 60nm.

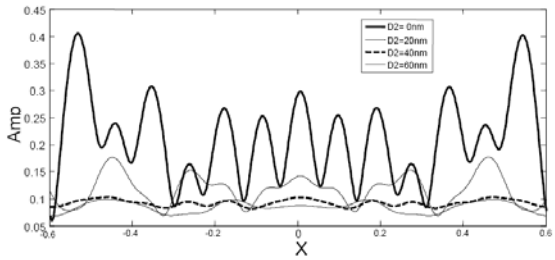

Fig. 14. The final comparison when D_1=80nm while D_2=0, 20, 40 and 60nm.

3.4 When silver slab separated 100nm from mask (i.e. D1=100nm)

The evanescent waves can not propagate to a long distance due to its exponential attenuation. The intensity of evanescent waves decays with a characteristic length Z_0 :

$$Z_0 = \frac{n}{k_t \sqrt{\sin^2 \theta_1 - n^2}} \tag{6}$$

where $n = n_2/n_1$ is the relative refractive index of two surrounding media; θ_1 is the incidence angle of light from optically denser media to optically thinner media; where $k_t = 2n_2\pi/\lambda$, λ is the wavelength of incident light. Theoretically, Z_0 can be 100nm by calculation.

In order to explore the potential imaging property of silver slab, we increased D1 as much as possible. Considering the evanescent waves may diminish when D_1=100nm, so we calculated the condition of D2=0nm only, the distribution of electromagnetic filed was shown in figure 15. It was found that the image of mask still can be resolved clearly in photoresist layer with good uniformity of imaged lines. We investigated the distribution of optical field in the 10nm cross-section of photoresist layer. The distribution of optical filed in the transverse section of photoresist was shown in figure 16. The image of mask can be resolved with high contrast. With proper choice of exposure condition and materials, the information of mask can be transferred to photoresist layer, and the image of mask can be reconstructed by the silver slab layer.

In brief, the image of mask can be transferred to the photoresist layer by the enhancement function of surface plasmon polaritons in silver slab. We calculated the 2D distribution of electromagnetic field in our model; the results showed that the image of mask with feature

size of 60nm line width can be resolved in photoresist layer when silver slab separated 100nm from mask. By proper design and choice of material, nanolithography with better resolution can be realized by the very function of silver slab, and this technique will be a possible alternative nanolithography technique for the next generation lithography.

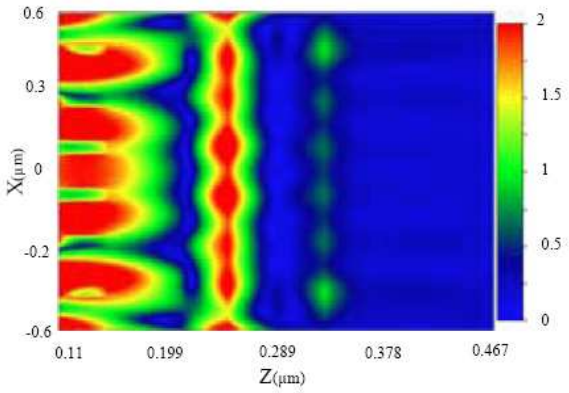

Fig. 15. The distribution of electromagnetic field in the model (Both X and Z is in unit of μm. Photoresist layer lies between Z=0.37μm and Z=0.47μm).

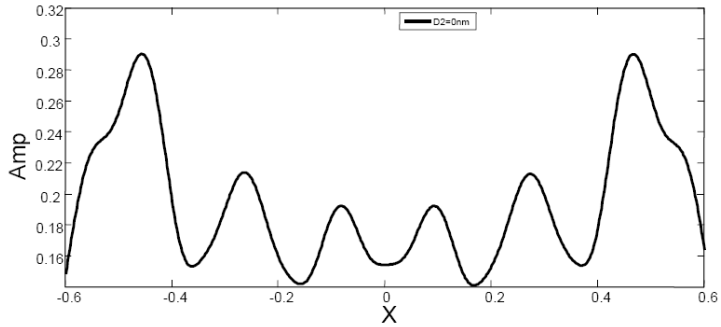

Fig. 16. The distribution of optical field in the 10nm cross-section of photoresist when silver slab separated 100nm from mask.

4. Conclusion

Two types of maskless lithography are discussed in this chapter. The first uses an array of high-numerical-aperture photon sieves as focusing elements in a scanning X-ray maskless nanolithography system. The system operating at wavelength of 0.5~2nm synchrotron light sources radiated, each of a large array of photon sieves focuses incident X-ray into a diffraction-limited on-axis nanoscale spot on the substrate coated photoresist. The X-ray intensity of each spot is modulated by means of a spatial light modulator. Patterns of arbitrary geometry are exposed and written in a dot matrix fashion while the substrate on a stepping stage is precisely driven in two dimensions according to the computer program.

The characteristics of synchrotron radiation light, resolution limits and depth of focus of the lithographic system are discussed. The design and fabrication of photon sieve are illustrated with a low-numerical-aperture amplitude-photon sieve fabricated on a chrome-coated quartz plate by means of laser-beam lithographic process, which minimum size of pinhole was 5.6um. The PSF of photon sieve in terms of side-lobes strength and main lobe width may be controlled by utilizing the apodization window function. The focusing performance of the photon sieve operating at wavelength of 632.8nm was simulated and tested. In combination with the synchrotron light sources, the photon sieve array X-ray maskless nanolithography is a promising tool in the nanometric device and special IC areas for the purpose of high resolution regardless of low yield.

The second focuses on the evanescent near field in nano-filmed noble metals. Sub-diffraction-limited feature size can be resolved by using i-line illumination exposure. Compared with the model of original superlens, we separated the superlens 100nm away from the mask, under the illumination of i-line light, the initial simulation shows that the sub-diffraction-limited feature as small as 60nm line width with 120nm pitch can be clearly resolved without hard contact between mask and nano-filmed noble metal. By proper design of the materials and the parameters of nano-filmed layers, better resolution can be realized.

In brief, a plasmonic structure for imaging and super focusing is a new approach besides the concept of negative refractive index. It is possible to realize imaging resolution beyond diffraction limit with a certain working distance within several wavelengths range. To realize this target, one of technical challenges is that how to transfer the high spatial frequency near-field signals from evanescent wave to propagation wave. The other challenge is that how to amplify the near-field evanescent wave from conventional ~200 nm to be $\sim 1\mu m$ or even several wavelengths in free space.

5. Acknowledgment

This work was supported by the grants from the Guangdong Natural Science Foundation (S2011040000711), the Key Lab of Robotics & Intelligent System, Guangdong Province (2009A060800016), the Guangdong & Chinese Academy of Sciences Cooperation Project (2009B091300160), National Natural Science Foundation of China (60904031; 60776029), Shenzhen Science & Technology Research Funds (2009-203), the Main Direction Program of the Knowledge Innovation of Chinese Academy of Sciences (KGCX2-YW-166), and the Scientific Research Foundation for the Returned Overseas Chinese Scholars of Ministry of Education, China (2008-890).

6. References

Blaikie, R.J., Melville, D.O.S. & Alkaisi, M. M. (2006). Super-resolution near-field lithography using silver lens: a review of recent developments. *Microelectronic Engineering*, Vol.83, No.4-9, pp.723-729, ISSN 0167-9317

Cao, Q., & Jahns, J. (2002). Focusing analysis of the pinhole photon sieve: individual far-field model. *J. Opt. Soc. Am. A*, Vol.19, No.12, pp.2387-2393, ISSN 0740-3232

Cao, Q., & Jahns, J. (2003). Nonparaxial model for the focusing of high-numerical-aperture photon sieves. *J. Opt. Soc. Am. A*, Vol.20, No.6, pp. 1005-1012, ISSN 0740-3232

Cheng, G. & Hu, C. (2011). X-ray Zernike apodized photon sieves for phase-contrast microscopy. *Acta Phys. Sin.* Vol.60, No.8, ISSN 1000-3290

Cheng, G., Hu, C., Xu P. & Xing, T. (2010). Zernike apodized photon sieves for high-resolution phase-contrast x-ray microscopy. *Opt. Lett.,* Vol.35, No.21, pp. 3610-3612, ISSN 0146-9592

Cheng, G., Xing, T., Yang, Y. & Ma, J. (2008). Resolution enhancement of photon sieve based on apodization. *Proc. SPIE,* Vol.6832, pp.83229-83229, ISBN 978-0-8194-7007-2, Beijing, China, Nov. 12-14, 2007

Cheng, G., Xing, T., Lin, W., Zhou, J., Qiu, C., Liao, Z., Yang, Y., Hong, L. & Ma, J. (2007). Photon sieve array x-ray maskless nanolithography. *Proc. SPIE,* Vol.6517, pp.51736-51736, ISBN 978-0-8194-6636-5, San Jose, CA, USA, Feb. 27-Mar. 01, 2007

Cheng, G., Xing, T., Yang, Y. & Ma, J. (2007). Experimental characterization of optical properties of photon sieve. *Proc. SPIE,* Vol.6724, pp.D7240-D7240, ISBN 978-0-8194-6881-9, Chengdu, China, Jul. 08-12, 2007

Cheng, G., Xing, T., Lin, W., Zhou, J., Qiu, C., Liao, Z. & Ma, J. (2006). Design and fabrication of low-numerical-aperture amplitude-photon sieve. *Chinese Journal of Sensors and Actuators*, Vol.19, No.5, pp.2344-2347, ISSN 1004-1699

Fang, N., Lee, H., Sun, C. & Zhang, X. (2005). Sub-diffraction-limited optical imaging with a silver superlens. *Science*, Vol.308, No.5721, ISSN 0036-8075

Kipp, L., Skibowski, M., Johnson, R. L., Berndt, R., Adelung, R., Harm, S. & Seemann, R. (2001) Sharper images by focusing soft X-rays with photon sieves. *Nature,* Vol.414, No.6860, pp. 184-188, ISSN 0028-0836

R. Menon, D. Gil, G. Barbastathis, and Smith, H. (2005). Photon-sieve lithography. *J. Opt. Soc. Am. A,* Vol.22, No.2, pp.342-345, ISSN 1084-7529

Yang, Y., Fu, Y., Yao, H., Hu, S., Zhou, S., Yan, W., Chen, W., Cheng, G. & Li, Z. (2009). Beam Splitter Achieved by Using Metallic Structure with Nanoslits. *J. Comput. Theor. Nanosci.*, Vol.6, No.5, pp.1030-1033, ISSN 1546-1955

Yang, Y., Hu, S., Yao, H., Cheng, G., Zhang, C. & Yan, W. (2007). Nanolithography in the Evanescent Near Field by Using Nano-filmed Noble Metal Layers. *Proc. SPIE,* Vol.6724, pp.A7241-A7241, ISBN 978-0-8194-6881-9, Chengdu, China, Jul. 08-12, 2007

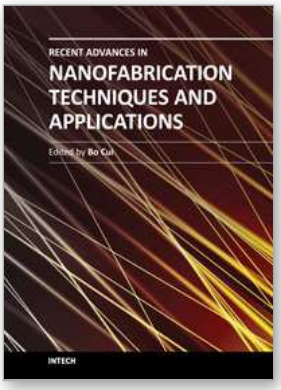

Recent Advances in Nanofabrication Techniques and Applications
Edited by Prof. Bo Cui

ISBN 978-953-307-602-7
Hard cover, 614 pages
Publisher InTech
Published online 02, December, 2011
Published in print edition December, 2011

Nanotechnology has experienced a rapid growth in the past decade, largely owing to the rapid advances in nanofabrication techniques employed to fabricate nano-devices. Nanofabrication can be divided into two categories: "bottom up" approach using chemical synthesis or self assembly, and "top down" approach using nanolithography, thin film deposition and etching techniques. Both topics are covered, though with a focus on the second category. This book contains twenty nine chapters and aims to provide the fundamentals and recent advances of nanofabrication techniques, as well as its device applications. Most chapters focus on in-depth studies of a particular research field, and are thus targeted for researchers, though some chapters focus on the basics of lithographic techniques accessible for upper year undergraduate students. Divided into five parts, this book covers electron beam, focused ion beam, nanoimprint, deep and extreme UV, X-ray, scanning probe, interference, two-photon, and nanosphere lithography.

How to reference
In order to correctly reference this scholarly work, feel free to copy and paste the following:

Guanxiao Cheng, Yong Yang, Chao Hu, Ping Xu, Helun Song, Tingwen Xing and Max Q.-H. Meng (2011). Emerging Maskless Nanolithography Based on Novel Diffraction Gratings, Recent Advances in Nanofabrication Techniques and Applications, Prof. Bo Cui (Ed.), ISBN: 978-953-307-602-7, InTech, Available from: http://www.intechopen.com/books/recent-advances-in-nanofabrication-techniques-and-applications/emerging-maskless-nanolithography-based-on-novel-diffraction-gratings

INTECH
open science | open minds

InTech Europe
University Campus STeP Ri
Slavka Krautzeka 83/A
51000 Rijeka, Croatia
Phone: +385 (51) 770 447
Fax: +385 (51) 686 166
www.intechopen.com

InTech China
Unit 405, Office Block, Hotel Equatorial Shanghai
No.65, Yan An Road (West), Shanghai, 200040, China
中国上海市延安西路65号上海国际贵都大饭店办公楼405单元
Phone: +86-21-62489820
Fax: +86-21-62489821